Carrier behavior in the vicinity of pit defects in GaN characterized by ultraviolet light-assisted Kelvin probe force microscopy

CuiHong Kai, XiaoJuan Sun, YuPing Jia, ZhiMing Shi, Ke Jiang, JianWei Ben, You Wu, Yong Wang, HeNan Liu, XiaoHang Li and DaBing Li

Articles you may be interested in

ZnO sheets prepared with a light-assisted growth method for improved photodegradation performance
Journal of Energy Chemistry **25**, 636 (2016);

A novel model of photo-carrier screening effect on the GaN-based p-i-n ultraviolet detector
SCIENCE CHINA Physics, Mechanics & Astronomy **53**, 793 (2010);

Design and implementation of precise position controller of active probe of atomic force microscopy for nanomanipulation

Chinese Science Bulletin **53**, 2090 (2008);

Investigation of Phase Behavior and Domain Structure of Phospholipid Monolayers by Atomic Force Microscopy
Chinese Science Bulletin **39**, 2076 (1994);

Adsorption behavior of hexadecyltrimethylammonium bromide (CTAB) to mica substrates as observed by atomic force microscopy
Science in China Series B-Chemistry **48**, 101 (2005);

Carrier behavior in the vicinity of pit defects in GaN characterized by ultraviolet light-assisted Kelvin probe force microscopy

CuiHong Kai[1,2], XiaoJuan Sun[1*], YuPing Jia[1], ZhiMing Shi[1], Ke Jiang[1,2], JianWei Ben[1,2], You Wu[1,2], Yong Wang[1,2], HeNan Liu[1], XiaoHang Li[3], and DaBing Li[1*]

[1]*State Key Laboratory of Luminescence and Applications, Changchun Institute of Optics, Fine Mechanics and Physics, Chinese Academy of Sciences, Changchun 130033, China;*
[2]*Center of Materials Science and Optoelectronics Engineering, University of Chinese Academy of Sciences, Beijing 100049, China;*
[3]*King Abdullah University of Science and Technology (KAUST), Advanced Semiconductor Laboratory, Thuwal 23955-6900, Saudi Arabia*

Surface potentials in the vicinity of V-pits (cone bottom) and U-pits (blunt bottom) on epitaxial GaN surface have been systematically studied using ultraviolet (UV) light-assisted Kelvin probe force microscopy (KPFM). The band structure models are established to understand variation of the surface potentials at the pits and planar surface with and without UV light. The photo-generated carrier behavior at the pit defects is studied. According to the surface potential results, it can be deduced that the carrier distributions around the V- and U-pits are uneven. In dark, the electron concentration at the bottom of V-pit ($30n_0$) and U-pit ($15n_0$) are higher than that at planar surface (n_0). Under UV light, for V-pit, the electron concentration at the cone bottom ($4.93\times10^{11}n_0$) is lower than that at the surrounding planar surface ($5.68\times10^{13}n_0$). For U-pit, the electron concentration at the blunt bottom is $1.35\times10^{12}n_0$, which is lower than that at the surrounding planar surface ($6.13\times10^{13}n_0$). The non-equilibrium electron concentrations at different locations are calculated. Based on the non-equilibrium electron concentration, it can be concluded that the carrier recombination rate at pit defects is higher than that at planar surface.

pit defects, surface potential, electron concentration

PACS number(s): 71.55.Eq, 61.72.Ff, 73.25.+i

1 Introduction

GaN and its alloys possess superior properties including adjustable and direct bandgap, large breakdown voltage, and high electron mobility. Thus, they are ideal for optoelectronic and power electronic devices, including light emitting diodes (LEDs), laser diodes and high-electron-mobility transistor [1-5]. However, high density of defects in GaN devices are common due to considerable lattice and thermal expansion mismatch between GaN and foreign substrates such as sapphire and silicon amid heteroepitaxy. Although defects are generally unfavorable that deteriorate device performance, pit-shape defects have been proven beneficial. Because if controlled properly, they have been shown to improve performance of InGaN/GaN multiple quantum well (MQW) LEDs, which are being employed and well-known by LED manufacturers. For instance, by introducing the pit defects, the InGaN/GaN MQW LED shows higher light emission

---

efficiency and lower leakage current [6]. Besides, the InGaN/GaN MQW LED with controlled V-shape pits (V-pits) exhibited higher internal quantum efficiency (IQE) of 80% than that without the V-pits (46%) [7]. Additionally, by increasing the size of the V-pit, the reverse leakage current of the InGaN/GaN LED was significantly reduced from 1.80 mA to 3.84 nA at −30 V [8]. Other studies show that the V-pits cause narrower sidewall MQWs and thus wider effective band gap, leading to potential barriers around defects, which prevent non-radiative recombination of electrons at the defect [9,10]. Recently, the benefits of the V-pit on performance of the InGaN/GaN LED have been confirmed by more researchers [11-13]. In comparison, similar effects have not been reported for AlGaN MQWs. For the AlGaN MQWs, the pit defects reportedly lower overall material quality and lead to a higher lateral inhomogeneity of material compositions and emission wavelength broadening [14,15]. Therefore, the effects of the pit defects on the carrier behavior have been investigated to understand and leverage the pit defects for the GaN devices. Up to now, the cathodoluminescence (CL) and Raman spectroscopy have been utilized to study carrier concentration in the GaN pit [16,17]. Besides, the conductive atomic force microscopy (C-AFM) has been employed to measure the leakage associated with the GaN pit [18]. However, most of the works focus on the influence V-pits on GaN without UV illumination or in dark. For the GaN based UV photoelectronic devices, understanding the carrier behavior of the pit under above-bandgap UV light illumination is significant to design and optimize the devices.

In this work, the surface potentials at GaN pit defects of two shapes, i.e. V- and U-pits, are studied by UV light-assisted KPFM in dark and under UV light. The photo-generated carrier transport behavior at the pit defects is discussed in detail. The carrier concentrations at V- and U-pit are calculated. Not only the results can lead to better understanding of the pit defects in GaN-based materials, but also they provide insights to improve performance of GaN-based devices.

2   Material and method

Metal organic chemical vapor deposition (MOCVD) was utilized to grow the GaN sample. Ammonia (NH₃) and tri-methylgallium (TMG) were N and Ga precursors, respectively. A 20-nm thick GaN buffer layer was firstly grown on a *c*-plane sapphire substrate at 635°C. The reactor pressure was 400 mbar. The V/III rate was 438. Then an undoped 5.5-μm thick GaN template was grown at 1080°C and the V/III rate was 808. The AFM (Bruker MultiMode-8 tapping mode) and the scanning electron microscope (SEM) (HITACHI S-4800) were employed to characterize the sample surface. The

pit density is about 8.9×10^6 cm^{-2} from SEM measurement (Figure 1). The KPFM (Bruker MultiMode-8 surface potential mode) was used to characterize the surface potential. The radius and elastic coefficient of the MESP model tip were 35 nm and 1-5 N/m, respectively. The scanner model of AFM and KPFM was AS-130VLR ("J" vertical).

3   Results and discussion

The morphologies of the pits were firstly measured by AFM. Two distinctive shapes of the pits, i.e. V- and U-pits are shown in Figure 2, in which the bottoms are cone-shaped and blunt, respectively. The depth profiles across the V- and U-pits are shown in Figure 2(b) and (d), respectively. The presence of the blunt bottom may be attributed to the generation of new planes at the bottom of the V-pit [19]. The plan-view SEM image of GaN epilayer is shown in Figure 1. The dodecagonal pyramid morphology has been observed,
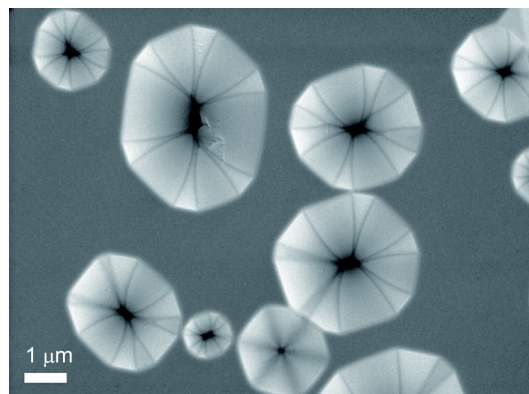

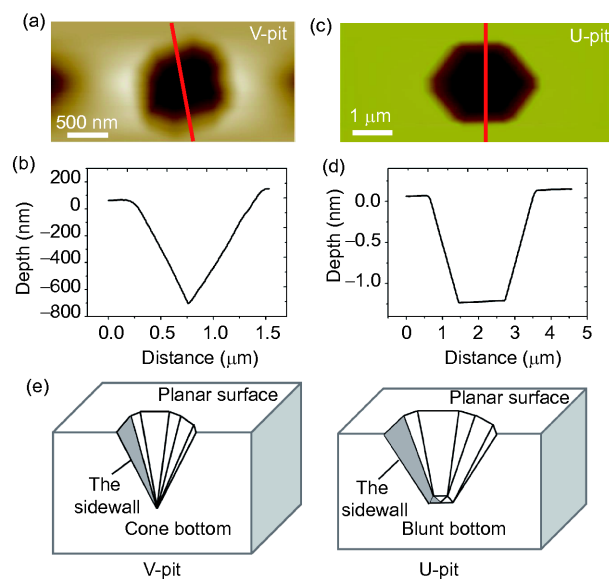**Figure 1**   SEM image of GaN epilayer filled with pit defects.

Figure 2   (Color online) (a) and (c) are AFM images of the V- and U-pits. (b) and (d) the section profiles along the red lines crossing the V- and U-pits in (a) and (c), respectively. (e) Schematic diagrams of V-pit and U-pit.

which is composed by {10$\bar{1}$1} and {11$\bar{2}$2} planes [20]. The schematic diagrams of the V- and U-pits are shown in Figure 2(e).

To study the carrier behavior, the surface potentials of the V- and U-pits in dark (Figure 3(a), (d)) and under UV light (Figure 3(b), (e)) were measured by UV assisted KPFM. Figure 3(c), (f) show the section profiles of surface potentials crossing the V- and U-pits in dark and under UV light, respectively. The results indicate that compared with the GaN planar surface, the surface potentials of both V- and U-pits are higher in dark but lower under UV light. However, there are some notable differences between the two pits. The cone bottom of the V-pit (Figure 3(c)) exhibits the highest surface potential in dark, i.e. 87 mV higher than that of the planar surface. Meanwhile, it shows the lowest surface potential under UV light, i.e. 122 mV lower than that of the planar surface. But for the U-pit (Figure 3(f)), the highest surface potential in dark (94 mV higher than that at planar), and the lowest one under UV light (129 mV lower than that at planar surface) are observed at the boundary between the bottom plane and the sidewall indicated by yellow arrows in Figure 3(d)-(f). The potentials at the bottom center of the U-pit is 24 mV lower in dark and 31 mV higher under UV light than those at the boundary. The surface potentials at planar surfaces under UV light are increased by 814 mV for the V-pit and 816 mV for the U-pit compared with those in dark.

The relationship of the surface potential (V_{DC}) and work functions of the sample (ϕ_{sample}) and the tip (ϕ_{tip}) can be written as eq. (1) [21],

$$V_{DC} = V_{sample} - V_{tip} = \frac{\phi_{tip} - \phi_{sample}}{e}, \qquad (1)$$

where $\phi_{sample}=\chi+(E_C-E_f)=\chi+E_n$. V_{sample} and V_{tip} are the surface potentials of the sample and the tip, respectively. χ is the electronic affinity, E_n is the difference between the conduction band minimum (E_C) and the Fermi level (E_f). According to eq. (1), the value of the E_n is inversely proportional to the surface potential. The schematic surface band diagrams can be drawn, as shown in Figure 4. The band change values at different positions in Figure 4 are calculated from the results of the KPFM measurements (Figure 3(c), (f)).

In the case of equilibrium, the electron concentration (n_{eq}) of semiconductor can be written as follows:

$$n_{eq} = N_C \exp\left(-\frac{E_C-E_f}{k_BT}\right) = N_C \exp\left(-\frac{E_n}{k_BT}\right), \qquad (2)$$

where N_C is the conduction band states density, k_B is the Boltzmann constant, T is room temperature (298 K).

The difference of the E_n between the V-pit and the planar surface is $E_{n(V\text{-}pit)}-E_{n(planar)}=-eV_1$, where V_1 (=87 mV) is the different surface potential at the V-pit and the planar surface. If the surface electron concentration at the planar surface in dark is set to n_0, the electron concentration ($n_{0V\text{-}pit}$) at the cone bottom in dark can be shown as eq. (3). According to eq. (3), it can be calculated that the electron concentration at the bottom of the V-pit is $30n_0$.

$$
\begin{aligned}
n_{0V\text{-}pit} &= N_C \exp\left(-\frac{E_{n(V\text{-}pit)}}{k_BT}\right) \\
&= N_C \exp\left(-\frac{E_{n(planar)}-eV_1}{k_BT}\right) \\
&= n_0 \exp\left(\frac{eV_1}{k_BT}\right). \qquad (3)
\end{aligned}
$$

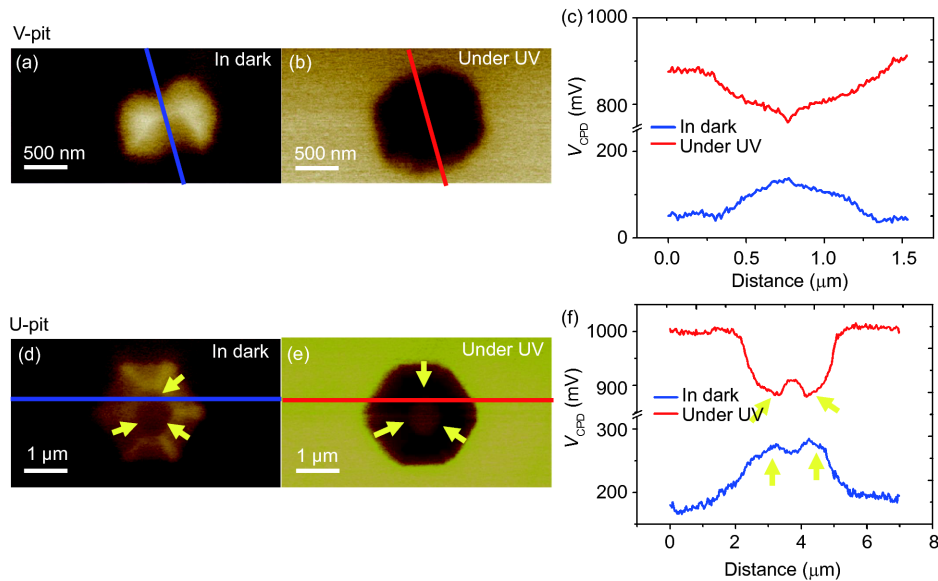Under UV illumination, the quasi-Fermi levels of electrons

Figure 3   (Color online) Surface potential images of the V- and U-pit obtained by KPFM: (a) and (d) in dark; (b) and (e) under UV light. (c) and (f) are section profile along the blue lines and red lines crossing the V- and U-pit. The position indicated by the yellow arrows in (d)-(f) is the boundary between the sidewall and the bottom of the U-pit.
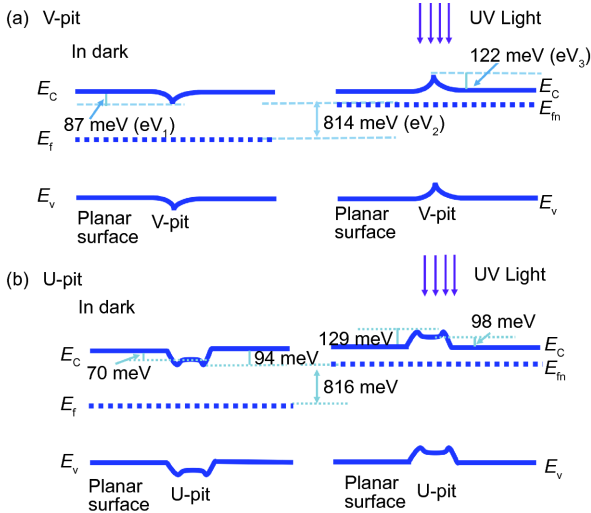
Figure 4   (Color online) Band diagrams in the vicinity of (a) the V-pit and (b) the U-pit in dark and under UV light.

Table 1   Electron concentrations at different positions of the V-pit in dark and under UV light

Positions	At planar surface (cm^{-3})	At the bottom of the V-pit (cm^{-3})
In dark	n_0	$30n_0$
UV light	$5.68\times10^{13}n_0$	$4.93\times10^{11}n_0$

(E_{fn}) and holes (E_{fp}) are separated rather than a unified Fermi level under equilibrium state. The electron concentration (n) of semiconductor is as follows:

$$n = N_C \exp\left(-\frac{E_C - E_{fn}}{k_B T}\right). \tag{4}$$

Under UV light, the electron can gather near sample surface, which results in the electron Fermi level at sample surface increased. The difference of electron's Fermi level in dark and under UV light can be written as $E_{fn} - E_f = eV_2$. V_2 is the surface potential difference between sample in dark and under UV light. Then, the electron concentration (n_L) at planar surface can be written as:

$$n_L = N_C \exp\left(-\frac{E_C - E_{fn}}{k_B T}\right) = n_0 \exp\left(\frac{eV_2}{k_B T}\right), \tag{5}$$

where V_2 is 814 mV. Then, n_L is calculated to be $5.68\times10^{13}n_0$. The surface electron concentration $n_{L(V\text{-pit})}$ at the cone bottom of the V-pit can be written as:

$$
\begin{aligned}
n_{L(V\text{-pit})} &= n\exp\left(-\frac{eV_3}{k_B T}\right) \\
&= n_0 \exp\left(\frac{eV_2}{k_B T}\right)\exp\left(-\frac{eV_3}{k_B T}\right),
\end{aligned} \tag{6}
$$

where V_3 (122 mV) is the surface potential difference between the bottom of the V-pit and the planar surface under UV light. According to eq. (6), $n_{L(V\text{-pit})}$ is calculated to be $4.93\times10^{11}n_0$. The electron concentration at different positions of V-pit with and without UV light are shown in Table 1.

At the blunt bottom of the U-pit, the surface band diagrams with and without UV light are shown in Figure 4(b). In dark, at the boundary of the bottom plane and the sidewall of the U-pit, the surface potential is 94 mV higher than that at the planar surface. So, the electron concentration at the boundary is $39n_0$ based on eq. (3). The surface potential at the bottom

plane is 70 mV higher than that at the planar surface, which means the electron concentration at the bottom plane is $15n_0$. Under UV light, the surface potential at planar surface is 816 mV higher than that in dark. According to eq. (5), the electron concentration at the planar surface under UV light is $6.13\times10^{13}n_0$. The difference of the potential between the bottom of the U-pit and the planar surface is 98 mV under UV light. According to eq. (6), the electron concentration at the bottom of the U-pit is $1.35\times10^{12}n_0$. Similarly, the surface potential at the boundary is 129 mV lower than that at planar surface, so the electron concentration at the boundary of the U-pit is $4.06\times10^{11}n_0$. The electron concentration at different positions of U-pit with and without UV light are shown in Table 2.

The non-equilibrium electron concentration (Δn) can be written as:

$$\Delta n = n - n_{eq} = (G - R)t, \tag{7}$$

where n_{eq} is the equilibrium carrier concentration; n is the electron concentration under UV light; G is the carrier generation rate, which is associated with illumination intensity and light absorption coefficient; R is the carrier recombination rate; t is the UV irradiation time. The non-equilibrium electron concentration Δn is inversely proportional to the carrier recombination rate R. For the V-pit, the non-equilibrium electron concentration Δn at the planar surface is $5.68\times10^{13}n_0 - n_0 \approx 5.68\times10^{13}n_0$. Δn at the cone bottom of V-pit is $4.93\times10^{11}n_0 - 30n_0 \approx 4.93\times10^{11}n_0$, which is smaller than that at the planar surface. Then, it can be concluded that the carrier recombination rate in the vicinity of the cone bottom is higher than that at the planar surface. It is reported that there is termination of threading dislocation at the cone bottom of the V-pit [22,23]. Since carrier mobility and lifetime are reduced due to carrier scattering at threading dislocation, the minority carrier diffusion length is lowered and thus the carrier recombination rate is larger than that in the area without dislocation, which is proven and confirmed by our UV assisted KPFM measurement and subsequent calculation of non-equilibrium electron concentration above

Table 2   Electron concentrations at different positions of the U-pit in dark and under UV light

Positions	At planar surface (cm^{-3})	At the bottom of the U-pit (cm^{-3})	At the boundary of the U-pit (cm^{-3})
In dark	n_0	$15n_0$	$39n_0$
UV light	$6.13\times10^{13}n_0$	$1.35\times10^{12}n_0$	$4.06\times10^{11}n_0$

[24,25]. A previous study also proved that the carrier re-combination rate at threading dislocation is 1.6 times larger than that at the GaN planar surface [26].

For the U-pit, a similar calculation process can be carried: Δn at planar surface is $6.13\times10^{13}n_0-n_0\approx6.13\times10^{13}n_0$; Δn at the boundary of the sidewall and bottom plane is $4.06\times10^{11}n_0-39n_0\approx4.06\times10^{11}n_0$. Δn at the boundary of the U-pit is smaller than that at the planar surface, which is consistent with that of the V-pit. The result also indicates that the boundary of the sidewall and bottom plane has lager carrier recombination rate than that at the planar surface. Similarly, it can be concluded that the carrier recombination rate at the bottom plane is higher than that at the planar surface but lower than that at the boundary. This may be attributed to the polarization characteristics of the bottom plane, which has a stronger spontaneous polarization than that at the sidewall, resulting in a lower carrier recombination rate than that at the sidewall of the U-pit. And the boundary of the sidewall and bottom plane is the junction of two crystal planes, which may have more dangling bond and defects than the perfect crystal plane, leading to a highest carrier recombination rate.

To further understand the variation of the surface potential with and without UV light, the band diagrams of the GaN planar surface and the pits in dark and under UV light are shown in Figure 5. In dark, at the GaN surface, the acceptor surface states lead to negative surface charges. Then, the hole will accumulate near the surface in a depletion region, which leads to a built-in electric field that points from the surface to the inside within the depletion region. It then leads to the energy band bending upward both at the planar surface and the pit surface, as shown in Figure 5(a) and (c), respectively. However, for the sidewalls of the V-and U-pit, which comprise $\{10\bar{1}1\}$ and $\{11\bar{2}2\}$ planes and have higher nitrogen (N) atom density than that on the (0001) plane, it is reported that the N-rich surfaces exhibited a high affinity towards oxygen (O) incorporation [27]. Therefore, the sidewalls of the V- and U-pit exhibit a higher O impurity incorporation than that on the (0001) plane. Since the O impurity on a N site behaves as shallow donors [28], it can partially compensate the acceptor surface states. The energy band upward bending will be less at the pit surface than that at the planar surface, leading to lower work function at the pit defects ($\Phi_{pit} < \Phi_{planar}$). As a result, the surface potentials at the V- and U-pit is higher than that at the planar surface in dark.

Under UV light, the photo-generated electron-hole pairs are separated by the built-in electric field. The electrons gather near GaN surface while the holes flow into the body. The band bending at the planar surface and the pit surface is less than that in dark. $\{10\bar{1}1\}$ and $\{11\bar{2}2\}$ planes are semi-polar with smaller polarization than that of (0001) plane. The weakened polarization leads to increased overlap of electron-hole wavefunctions and thus the probability of carrier re-
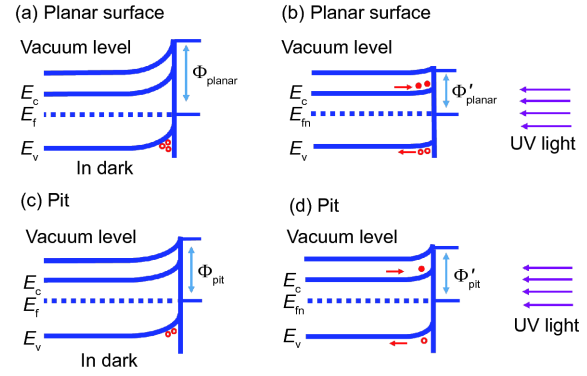

Figure 5   (Color online) Band diagrams of the planar surface (a) in dark and (b) under UV light. Band diagrams of the pits (c) in dark and (d) under UV light.

combination [29]. As a result, the recovery of upward band bending at the pit is less than that at the planar surface. Then, the work function of the pit is higher than that of planar surfaces ($\Phi'_{pit} > \Phi'_{planar}$). As a result, the surface potentials at the V- and U-pits are lower than that at planar surfaces, as shown by the KPFM measurement (Figure 3(b) and (e)). Therefore, the higher carrier recombination of the pits than that of planar surface can be observed directly by UV light-assisted KPFM, which exhibits a convenient way to identify the carrier recombination behavior of pits in III-nitride materials and structures.

4   Conclusions

In summary, the surface potentials in the vicinity of the V- and U-pit are studied by UV light-assisted KPFM. The results indicate that the pits cause uneven distribution of carriers on the GaN surface. For the V-pit, the extreme points of surface electron concentration appear at the cone bottom. In dark, the electron concentrations at the planar surface and the cone bottom are n_0 and $30n_0$, respectively. Under UV light, the electron concentration is $5.68\times10^{13}n_0$ at planar surface and $3.45\times10^{12}n_0$ at the cone bottom. For the U-pit, the highest electron concentration in dark and lowest electron concentration under UV light are observed at the boundary between the bottom plane and the sidewall. The electron concentration at boundary is $39n_0$ in dark. Under UV light, it is $6.13\times10^{13}n_0$ at planar surface and $1.21\times10^{12}n_0$ at the boundary. At the same time, the carrier recombination rate at the V- and U-pit is higher than that at the planar surface. The band models of planar surface and pits in dark and under UV light are proposed to explain the variation of the surface potentials. The results facilitate better understanding of the pit defect for device performance optimization. It also shows that the UV assisted KPFM is an effective way to obtain the carrier recombination behavior of III-nitride materials and structures.

1 D. Li, K. Jiang, X. Sun, and C. Guo, Adv. Opt. Photon. **10**, 43 (2018).
2 S. H. Lim, Y. H. Ko, C. Rodriguez, S. H. Gong, and Y. H. Cho, Light Sci. Appl. **5**, e16030 (2016).
3 E. Matioli, S. Brinkley, K. M. Kelchner, Y. L. Hu, S. Nakamura, S. DenBaars, J. Speck, and C. Weisbuch, Light Sci. Appl. **1**, e22 (2012).
4 L. X. Zhao, S. C. Zhu, C. H. Wu, C. Yang, Z. G. Yu, H. Yang, and L. Liu, Sci. China-Phys. Mech. Astron. **59**, 107301 (2016).
5 Y. Huang, P. X. Li, Z. Yang, Y. Hao, and X. B. Wang, Sci. China-Phys. Mech. Astron. **57**, 887 (2014).
6 H. Takahashi, A. Ito, T. Tanaka, A. Watanabe, H. Ota, and K. Chikuma, Jpn. J. Appl. Phys. **39**, L569 (2000).
7 I. A. Ajia, P. R. Edwards, Y. Pak, E. Belekov, M. A. Roldan, N. Wei, Z. Liu, R. W. Martin, and I. S. Roqan, ACS Photon. **5**, 820 (2018).
8 J. Kim, J. Kim, Y. Tak, S. Chae, J. Y. Kim, and Y. Park, IEEE Electron. Device Lett. **34**, 1409 (2013).
9 A. Hangleiter, F. Hitzel, C. Netzel, D. Fuhrmann, U. Rossow, G. Ade, and P. Hinze, Phys. Rev. Lett. **95**, 127402 (2005).
10 M. K. Kim, S. Choi, J. H. Lee, C. H. Park, T. H. Chung, J. H. Baek, and Y. H. Cho, Sci. Rep. **7**, 42221 (2017).
11 D. Han, S. Ma, Z. Jia, W. Jia, P. Liu, H. Dong, L. Shang, A. Zhang, G. Zhai, X. Li, X. Liu, and B. Xu, J. Phys. D-Appl. Phys. **50**, 475103 (2017).
12 K. Sugimoto, N. Okada, S. Kurai, Y. Yamada, and K. Tadatomo, Jpn. J. Appl. Phys. **57**, 062101 (2018).
13 S. W. Chen, H. Li, C. J. Chang, and T. C. Lu, Materials **10**, 113 (2017).
14 X. Li, G. Le Gac, S. Bouchoule, Y. El Gmili, G. Patriarche, S. Sundaram, P. Disseix, F. Réveret, J. Leymarie, J. Streque, F. Genty, J. P. Salvestrini, R. D. Dupuis, X. H. Li, P. L. Voss, and A. Ougazzaden, J. Cryst. Growth **432**, 37 (2015).
15 J. Jeschke, M. Martens, A. Knauer, V. Kueller, U. Zeimer, C. Netzel, C. Kuhn, F. Krueger, C. Reich, T. Wernicke, M. Kneissl, and M. Weyers, IEEE Photon. Technol. Lett. **27**, 1969 (2015).
16 M. Zhang, D. Cai, Y. Zhang, X. Su, T. Zhou, M. Cui, C. Li, J. Wang, and K. Xu, Mater. Lett. **198**, 12 (2017).
17 T. Paskova, E. M. Goldys, and B. Monemar, J. Cryst. Growth **203**, 1 (1999).
18 A. Lochthofen, W. Mertin, G. Bacher, L. Hoeppel, S. Bader, J. Off, and B. Hahn, Appl. Phys. Lett. **93**, 022107 (2008).
19 W. Lee, H. J. Lee, S. H. Park, K. Watanabe, K. Kumagai, T. Yao, J. H. Chang, and T. Sekiguchi, J. Cryst. Growth **351**, 83 (2012).
20 E. Richter, U. Zeimer, F. Brunner, S. Hagedorn, M. Weyers, and G. Tränkle, Phys. Status Solidi C **7**, 28 (2010).
21 D. B. Li, X. J. Sun, Y. P. Jia, M. I. Stockman, H. P. Paudel, H. Song, H. Jiang, and Z. M. Li, Light Sci. Appl. **6**, e17038 (2017).
22 K. Watanabe, J. R. Yang, S. Y. Huang, K. Inoke, J. T. Hsu, R. C. Tu, T. Yamazaki, N. Nakanishi, and M. Shiojiri, Appl. Phys. Lett. **82**, 718 (2003).
23 K. S. Son, D. G. Kim, H. K. Cho, K. Lee, S. Kim, and K. Park, J. Cryst. Growth **261**, 50 (2004).
24 L. Chernyak, A. Osinsky, G. Nootz, A. Schulte, J. Jasinski, M. Benamara, Z. Liliental-Weber, D. C. Look, and R. J. Molnar, Appl. Phys. Lett. **77**, 2695 (2000).
25 A. Cavallini, L. Polenta, and A. Castaldini, Microelectron. Reliab. **50**, 1398 (2010).
26 Z. Liu, K. Xu, Y. Fan, G. Xu, Z. Huang, H. Zhong, J. Wang, and H. Yang, Appl. Phys. Lett. **101**, 252107 (2012).
27 N. A. Fichtenbaum, T. E. Mates, S. Keller, S. P. DenBaars, and U. K. Mishra, J. Cryst. Growth **310**, 1124 (2008).
28 D. Meister, M. Böhm, M. Topf, W. Kriegseis, W. Burkhardt, I. Dirnstorfer, S. Rösel, B. Farangis, B. K. Meyer, A. Hoffmann, H. Siegle, C. Thomsen, J. Christen, and F. Bertram, J. Appl. Phys. **88**, 1811 (2000).
29 P. Waltereit, O. Brandt, A. Trampert, H. T. Grahn, J. Menniger, M. Ramsteiner, M. Reiche, and K. H. Ploog, Nature **406**, 865 (2000).